Electron−Rotor Interaction in Organic−Inorganic Lead Iodide Perovskites Discovered by Isotope Effects

HPSTAR
222-2016

Jue Gong,[†,#] Mengjin Yang,[‡,#] Xiangchao Ma,[§] Richard D. Schaller,[‖] Gang Liu,*[⊥] Lingping Kong,[⊥] Ye Yang,[‡] Matthew C. Beard,[‡] Michael Lesslie,[†] Ying Dai,[§] Baibiao Huang,[§] Kai Zhu,*[‡] and Tao Xu*[†]

[†]Department of Chemistry and Biochemistry, Northern Illinois University, DeKalb, Illinois 60115, United States
[‡]Chemistry and Nanoscience Center, National Renewable Energy Laboratory, Golden, Colorado 80401, United States
[§]School of Physics, State Key Laboratory of Crystal Materials, Shandong University, Jinan 250100, China
[‖]Center for Nanoscale Materials, Argonne National Laboratory, Argonne, Illinois 60439, United States
[⊥]Center for High Pressure Science and Technology Advanced Research, Shanghai 201203, China

S Supporting Information

ABSTRACT: We report on the carrier−rotor coupling effect in perovskite organic−inorganic hybrid lead iodide ($CH_3NH_3PbI_3$) compounds discovered by isotope effects. Deuterated organic−inorganic perovskite compounds including $CH_3ND_3PbI_3$, $CD_3NH_3PbI_3$, and $CD_3ND_3PbI_3$ were synthesized. Devices made from regular $CH_3NH_3PbI_3$ and deuterated $CH_3ND_3PbI_3$ exhibit comparable performance in band gap, current−voltage, carrier mobility, and power conversion efficiency. However, a time-resolved photoluminescence (TRPL) study reveals that $CH_3NH_3PbI_3$ exhibits notably longer carrier lifetime than that of $CH_3ND_3PbI_3$, in both thin-film and single-crystal formats. Furthermore, the comparison in carrier lifetime between $CD_3NH_3PbI_3$ and $CH_3ND_3PbI_3$ single crystals suggests that vibrational modes in methylammonium (MA^+) have little impact on carrier lifetime. In contrast, the fully deuterated compound $CD_3ND_3PbI_3$ reconfirmed the trend of decreasing carrier lifetime upon the increasing moment of inertia of cationic MA^+. Polaron model elucidates the electron−rotor interaction.
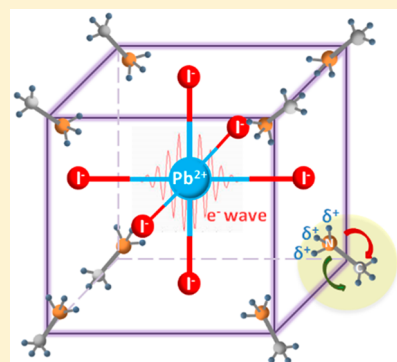
Charge carrier−lattice interaction regulates a wide range of material properties and governs the underlying working principles of various energy materials.[1,2] Thus, basic understandings of any new type of carrier−lattice interaction is exceptionally desirable for accomplishing the mechanistic foundation of modern material science. In solid-state physics, electron−lattice interaction is typically exemplified by the interplay between electrons and lattice vibration, namely, electron−phonon interaction.[3−10] However, the emerging organic−inorganic hybrid lead iodide perovskite materials (e.g., $CH_3NH_3PbI_3$ or noted as $MAPbI_3$) offers a new platform to explore some unusual fundamental interactions between carriers and lattice. Particularly, a unique feature in organic−inorganic hybrid lead iodide perovskite compounds is that the organic cations—for example, the most representative methylammonium (MA^+)—also undergoes rotational motions.[11−17] Explicitly, the monocationic charge on MA^+ is localized on the three ammonium hydrogen atoms due to the much larger electronegative nature of the nitrogen atom, thus forming a geometrically asymmetric cationic rotor in the cages constituted by the inorganic PbI_3^- framework. At room temperature, this cationic rotor experiences two rapid and asymmetric in-plane rotational modes that take ~3 ps to rotate 90° around the center of the cation with a small rotational energy barrier (1.3 kJ/mol), as well as a symmetric axial rotation along the C−N

bond with a period of as fast as ~300 fs.[18−20] Consequently, the structure of hybrid lead iodide perovskite materials can be pictured as the individual cationic organic rotors electrostatically pinned in the cages of a solid-state anionic inorganic framework. Because the valence band of $MAPbI_3$ is mainly formed by I 5p orbitals with a minor contribution from Pb 6s orbitals and the conduction band is composed of Pb 6p orbitals,[21−24] photoinduced electrons and holes should reside in the inorganic PbI_3^- framework. As such, it becomes intriguing to investigate at a fundamental level how photo-induced carriers in the inorganic framework interplay with neighboring cationic organic rotors, which may cause a kinetic perturbation on the conduction electron wave function, as depicted in Figure 1. Such an effort should help to build a solid theoretical foundation in the quest for better photovoltaic materials-by-design that can overcome constraints such as lead toxicity and instability issues.[25−30] Here, we substitute all three hydrogens on organonitrogen and/or the organocarbon with deuterium atoms to modulate the rotational frequency of the MA^+ cation while keeping its own molecular polarity and electronic wave function intact. We have unambiguously
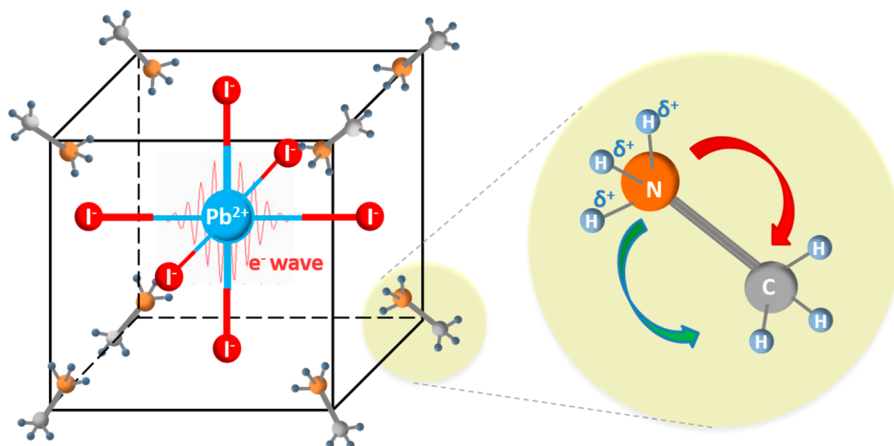
Figure 1. Schematic depiction of the $CH_3NH_3^+$ cationic rotors in the cage formed by the anionic PbI_3^- framework. The rotors undergo two in-plane rotations around the C−N axis, which can alter the electrostatic attraction between the nearby three positive-charged H atoms and the photoinduced conduction electron wave function in the PbI_3^- framework.

observed the isotope effect on the interplay between electrons and rotors, as evidenced by the deuterium-modulated carrier lifetime in hybrid perovskite materials. Moreover, exciton binding energies and polaron trapping energies associated with different crystallographic planes were calculated based on the orientations of the MA^+ rotor, which clearly exhibits strong dependence on the MA^+ orientations.

Figure 2a shows the ultraviolet−visible (UV−vis) absorbance of the thin films for both $CH_3NH_3PbI_3$ and $CH_3ND_3PbI_3$. (See the Experimental Methods section for synthesis and Figures S1−S5 and Figure S6 for nuclear magnetic resonance (NMR) and mass spectra, respectively, of CH_3NH_3I, CH_3ND_3I, CD_3NH_3I, and CD_3ND_3I.) Note that the thin films of $CH_3NH_3PbI_3$ and $CH_3ND_3PbI_3$ exhibit comparable film quality

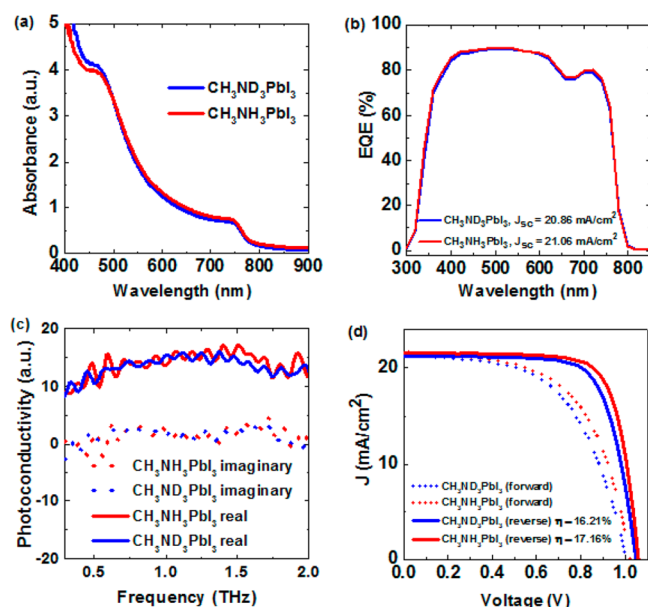**Figure 2.** (a) UV−vis absorbance spectrum for both perovskites with their absorption edge onsets. Blue, $CH_3ND_3PbI_3$; red, $CH_3NH_3PbI_3$. (b) IPCE spectra for $CH_3NH_3PbI_3$ and $CH_3ND_3PbI_3$. Blue curve, $CH_3ND_3PbI_3$; red, $CH_3NH_3PbI_3$. (c) Terahertz measurements for $CH_3NH_3PbI_3$ and $CH_3ND_3PbI_3$. Red curve, $CH_3NH_3PbI_3$; blue, $CH_3ND_3PbI_3$. (d) Hybrid lead iodide-based solar cells' J−V characteristics. Red curves, $CH_3NH_3PbI_3$; blue curves, $CH_3ND_3PbI_3$.

in terms of crystallinity and morphology, as evidenced by both X-ray diffraction (XRD) and scanning electron microscopy (SEM) (Figures S7 and S8, respectively). The onsets of the absorption edges for both spectra nearly overlap and occur at about 787 nm, which corresponds to a 1.575 eV band gap for $CH_3NH_3PbI_3$, and at about 788 nm, which corresponds to a 1.573 eV band gap for $CH_3ND_3PbI_3$. A complete UV−vis absorbance study was performed on $CH_3NH_3PbI_3$, $CH_3ND_3PbI_3$, $CD_3NH_3PbI_3$, and $CD_3ND_3PbI_3$ thin films, and their absorption edge onsets are shown to closely overlap at 825 nm (Figure S9). Previous reports show that the band gap of semiconductors can be influenced by isotope effects when the isotope atoms are relevant to the band structure. For example, the replacements of Cu-63 with Cu-65 and/or Cl-35 with Cl-37 in a CuCl crystal alter the band gap through electron−phonon interaction due to the mass-induced change in lattice dynamical properties.[31] Electron−phonon coupling induced by isotopic effects is also shown to distinctively manipulate optoelectronic properties of conducting polymers, which have different optoelectronic responses when hydrogen atoms on the main chain or side chain are replaced by deuterium atoms.[32] However, for organic−inorganic hybrid perovskite materials, the band gap is dominated by the inorganic PbI_3^- framework. Thus, the substitution of hydrogen with deuterium on the MA^+ does not alter the lattice vibration in the PbI_3^- network, in which the band gap transition accounts as a major transition from the I 5p to Pb 6p orbital, with minor transition from the Pb 6s to Pb 6p orbital.[21−24] On the other hand, electronic transition from I 5p to Pb 6p does not involve a change of angular momentum quantum number ($l = 1$), and the transition from Pb 6s to Pb 6p does not involve a change of the principal quantum number ($n = 6$); therefore, regular perovskite $CH_3NH_3PbI_3$ exhibits excellent absorption. This property is well kept by $CH_3ND_3PbI_3$, as evidenced by the nearly overlapped UV−vis spectra of $CH_3NH_3PbI_3$ and $CH_3ND_3PbI_3$ because the substitution of H with D in MA^+ does not influence the quantum numbers of the electronic transitions in the PbI_3^- framework.

We then further investigate the isotope effects of MA^+ on the light-harvesting and charge-generation/collection process by studying the incident photon-to-electron conversion efficiency (IPCE) of both $CH_3NH_3PbI_3$- and $CH_3ND_3PbI_3$-based thin films, as illustrated in Figure 2b. The film qualities (e.g.,

crystallinity, grain size, film coverage) of both $CH_3NH_3PbI_3$ and $CH_3ND_3PbI_3$ are comparable, as indicated in Figures S7 and S8. The IPCE spectra of perovskite solar cells based on $CH_3NH_3PbI_3$ and $CH_3ND_3PbI_3$ thin films agree well with each other. The comparable IPCE and absorption spectra of $CH_3NH_3PbI_3$- and $CH_3ND_3PbI_3$-based devices suggest that the isotope of the MA^+ does not affect the generation and subsequent collection of photocarriers. This is consistent with the fact that the photogeneration of electron−hole pairs occurs in the PbI_3^- framework and is thus expected to be independent of MA^+.

In addition, we used time-resolved terahertz (THz) spectroscopy to investigate the influence of isotope effects of MA^+ on the charge-carrier mobility in the perovskite thin films ($CH_3NH_3PbI_3$ and $CH_3ND_3PbI_3$). Again, the comparable film quality in terms of morphology and crystallinity is indicated by SEM and XRD (Figures S7 and S8). As shown in Figure 2c, both samples show nearly constant real photoconductivity and zero imaginary photoconductivity, implying a large carrier-scattering frequency.[33] Compared with conventional photovoltaic semiconductors, the carrier mobility ($1-10$ cm^2 V^{-1} S^{-1})[34−37] in perovskite is relatively low because of this large carrier-scattering frequency. The scattering in perovskites is likely dominated by the carrier−optical phonon interaction that is also responsible for the effective hot-phonon bottleneck.[38] This frequency-independent photoconductivity (in the low-THz frequency region) is also in agreement with the reported measurements for different perovskite films.[35,39] Considering the similar photocarrier densities due to the identical excitation condition, the comparable photoconductivities between $CH_3NH_3PbI_3$ and $CH_3ND_3PbI_3$ thin films suggest similar carrier mobilities in these two films. This phenomenon agrees with the fact that carrier mobility is primarily determined by the carrier−optical phonon interaction, electron−hole Coulomb interaction, and effective mass, which are all inherent to the inorganic PbI_3^- framework. Thus, the carrier mobility measured by the THz study is expected to be independent of the organic MA^+.

Figure 2d compares the photocurrent density−voltage ($J-V$) characteristics of perovskite solar cells based on $CH_3NH_3PbI_3$ and $CH_3ND_3PbI_3$ thin films; note that these cells were prepared under the same condition and care was taken to ensure no replacement of deuterium with hydrogen by avoiding the use of any solvent with active hydrogen (see the Experimental Methods section). Both cells exhibit comparable photovoltaic performance. The best $CH_3NH_3PbI_3$-based device displays a PCE of 17.15% with a short-circuit photocurrent density (J_{sc}) of 21.57 mA/cm^2, open-circuit voltage (V_{oc}) of 1.06 V, and fill factor (FF) of 0.75. In contrast, the best $CH_3ND_3PbI_3$-based device has an efficiency of 16.27% with J_{sc} of 21.22 mA/cm^2, V_{oc} of 1.05 V, and FF of 0.73. The slight difference in these photovoltaic parameters between the best $CH_3NH_3PbI_3$ and $CH_3ND_3PbI_3$ devices is similar to a statistical comparison based on the 8−10 devices from each material (Table S1). It is evident that both devices exhibit a similar hysteretic $J-V$ behavior, as commonly observed for standard $CH_3NH_3^+$-based perovskite solar cells.[40] For the $CH_3ND_3^+$-based device, we examined its steady-state power output biased near the maximum power point under a continuous light illumination over a few minutes (Figure S10). The measurement shows that the actual power output (15.4%) for deuterated film is close to its reverse-scan curve. Because there is no significant change of carrier mobility for the

deuterated film, carrier recombination could be accounted for by the slight but evident deterioration in performance.

We conducted time-resolved photoluminescence (TRPL) measurements to examine charge-carrier lifetime as commonly used for $CH_3NH_3PbI_3$, as reported in the literature.[41−43] Strikingly, TRPL reveals a significant difference in carrier lifetimes of the $CH_3NH_3PbI_3$ thin film (~145 ns) and $CH_3ND_3PbI_3$ thin film (~91 ns), as shown in Figure 3a,b.
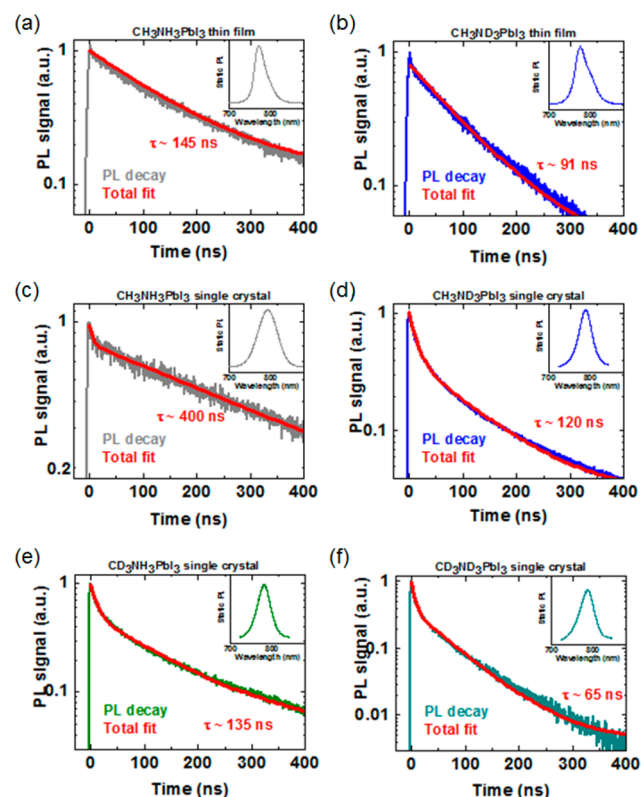
Figure 3. (a) TRPL of a $CH_3NH_3PbI_3$ thin film; (b) TRPL of a $CH_3ND_3PbI_3$ thin film; (c) TRPL of single-crystal $CH_3NH_3PbI_3$; (d) TRPL of single-crystal $CH_3ND_3PbI_3$; (e) TRPL of single-crystal $CD_3NH_3PbI_3$; and (f) TRPL of single-crystal $CH_3ND_3PbI_3$. The insets are the static photoluminescence spectra.

To minimize the possible influence due to morphological defects in thin films, single crystals of both $CH_3NH_3PbI_3$ and $CH_3ND_3PbI_3$ were synthesized, and their crystallinities were examined by SEM of the cleaved crystal surface and synchrotron high-resolution XRD at the Advanced Photon Source (see the Experimental Methods section and Figure S11). Clearly, the TRPL comparison between single-crystal $CH_3NH_3PbI_3$ (Figure 3c) and single-crystal $CH_3ND_3PbI_3$ (Figure 3d) echoes the results obtained from the thin-film study, namely, that the carrier lifetime in the $CH_3NH_3PbI_3$ single crystal (400 ns) is still much longer than that of the $CH_3ND_3PbI_3$ single crystal (~135 ns). It is not surprising that single crystals generally have longer carrier lifetime than their corresponding thin films because single crystals should exhibit much less nonradiative recombination from structure-induced defect centers.

To find the root cause of this isotope effect on carrier lifetime, we conduct a logical reasoning: first of all, the observed isotope effect of MA^+ on the carrier lifetime must be implemented through a mass-relevant interaction(s) between

Table 1. Dielectric Constants for MAPbI$_3$ When the C−N Axial of MA$^+$ Is Pointing in Different Crystallographic Directions[a]

100			110			111		
14.227	−0.053	0.387	25.016	4.551	−0.140	25.700	2.151	−2.451
−0.053	17.722	0.111	4.552	24.265	−0.629	2.152	25.477	2.237
0.391	0.111	17.850	−0.140	−0.629	20.936	−2.449	2.235	25.800
16.600 (averaged)			23.406 (averaged)			25.659 (averaged)		

[a]Note that for a nonperfect isotropic structure, its dielectric constant is a second-order tensor; thus, the dielectric constant is a 3 × 3 matrix, while the averaged diagonal dielectric constants are also given in the last row.

the MA$^+$ and the photoinduced carriers in the inorganic PbI$_3^-$ framework because deuteration should not alter any steady-state electronic wave functions on the MA$^+$ or PbI$_3^-$ framework. Hence, there can only be two possible mass-relevant properties to influence the interaction between MA$^+$ and the carriers in the PbI$_3^-$ framework, including the vibrational and rotational modes of MA$^+$. Note that we eliminated the translational modes of MA$^+$ in our consideration because the cationic MA$^+$ is confined electrostatically by the surrounding anionic PbI$_3^-$ framework.[20,44,45] As expected, the infrared study shows that the characteristic broad N−H stretching at ~3150 cm^{-1} disappeared almost entirely in CH$_3$ND$_3$PbI$_3$ (Figure S12) in single-crystal format. Furthermore, the infrared spectra of CD$_3$NH$_3$PbI$_3$ and CD$_3$ND$_3$PbI$_3$ thin films are shown in Figure S13. At this point, we can say that (1) the carrier lifetime may be related to the vibrational difference between N−H and N−D or (2) the carrier lifetime may be related to the total mass of the MA$^+$ because CH$_3$NH$_3$ is lighter than CH$_3$ND$_3$. We then need to either rule out or confirm the impact of vibrational modes in MA$^+$ on carrier lifetime. If the N−H vibrations have any strong impact on carrier lifetime, we should be able to see the difference between CH$_3$ND$_3^+$ and CD$_3$NH$_3^+$ while eliminating the impact due to the overall mass of the MA$^+$ because CH$_3$ND$_3^+$ and CD$_3$NH$_3^+$ have the same mass. Thus, we further synthesized the single crystal of CD$_3$NH$_3$PbI$_3$, which adds the same amount of mass to the organic cation as the aforementioned CH$_3$ND$_3$PbI$_3$ while keeping the N−H vibrational mode intact. The quality of the CD$_3$NH$_3$PbI$_3$ sample is confirmed by SEM of the cleaved crystal surface and synchrotron high-resolution XRD (see the Experimental Methods section and Figure S11). As can be seen from Figure 3e, CD$_3$NH$_3$PbI$_3$ exhibits a carrier lifetime of ~135 ns, very close to that of CH$_3$ND$_3$PbI$_3$ (~120 ns; see Figure 3d). These results suggest that the vibrational modes in −NH$_3^+$, deuterated −ND$_3^+$, −CH$_3$, or CD$_3$ do not notably impact carrier lifetime. Instead, the overall mass of MA$^+$ leads to the variation in carrier lifetime. To further verify the impact of MA$^+$ mass on the carrier lifetime, we synthesized the fully deuterated single-crystal CD$_3$ND$_3$PbI$_3$, and its crystallinity is also comparable with other crystals, as confirmed by SEM of the cleaved crystal surface and synchrotron high-resolution XRD (see the Experimental Methods section and Figure S11). Figure 3f shows that the carrier lifetime of this fully deuterated CD$_3$ND$_3$PbI$_3$ single-crystal sample is only ~65 ns as measured by TRPL, which is much shorter than that for either CD$_3$NH$_3$PbI$_3$ or CH$_3$ND$_3$PbI$_3$ single crystals and confirms our hypothesis of the effect of MA$^+$ mass on carrier lifetime.

Clearly, to this point, we need to focus the search for the root cause of this isotope-induced carrier-lifetime variation on the rotational modes of MA$^+$. According to the unit cell dimensions of MAPbI$_3$ single crystals (8.8310 × 8.8310 × 12.6855 Å^3),[22,37,46,47] the concentration of MA$^+$ is 10^{21}/cm^3, which overwhelmingly outnumbers the intrinsic charge-carrier density

(about 10^{10} cm^{-3} under dark,[37] in the PbI$_3^-$ framework) by 11 orders of magnitude. Even under our TRPL condition (excitation at 405 nm, 40 pJ/pulse, 200 μm spot size), the estimated initial carrier density is no more than 10^{14} cm^{-3}, which is still 7 orders of magnitude lower than the number of MA$^+$ rotors. As such, the time-dependent wave function of these "rarely" occurring photoinduced electrons in the PbI$_3^-$ framework have a slight chance to overlap with the anisotropically positioned cationic charge on the neighboring MA$^+$, if all of the MA$^+$ are randomly oriented but fixed in the PbI$_3^-$ cages. In other words, due to the relatively low carrier concentration, the interaction between an electron in the conduction band (Pb 6p orbitals) and the cationic side of a neighboring MA$^+$ requires a rapid reorientation of this MA$^+$ to have its positive charge pointed to the electron; this occurrence enhances the overlapping probability of their respective wave functions. Such a requirement apparently demands the rotational movement of the MA$^+$. In fact, MA$^+$ does experience rotational modes in the PbI$_3^-$ framework, including a symmetric axial rotation along the C−N bond that does not alter the overall orientation of MA$^+$; in addition, there are two asymmetric in-plane rotations, which spatially reorient the charge on MA$^+$ with respect to the nearby carrier. Such interaction also requires a timely coupling. In fact, all of these rotational modes occur at a time scale no longer than a few tens of picoseconds, which is 2−4 orders of magnitude faster than the carrier lifetime. Hence, the reorientation of MA$^+$ is kinetically rapid enough to enhance the probability of transient overlap between the wave functions of electrons in the conduction band and the positive charge on MA$^+$. In this regard, the modulation of the rotational frequency of MA$^+$ by isotope effects is a logical interpretation of the observed mass-dependent carrier lifetime.

In general, carrier lifetime is closely associated with the exciton binding energy and polaron trapping energy. In terms of excitons, a larger binding energy generally leads to a higher recombination rate, partially owing to the stronger Coulomb interaction. Theoretically, we can estimate the exciton binding energy by eq 1[48]

$$E(b) = \frac{\mu}{m_0 \varepsilon_r^2} R_H \tag{1}$$

where m_0 is the free-electron mass, R_H is the Rydberg constant of a hydrogen atom (13.6 eV), ε_r is the dielectric constant of the material, and μ is the reduced effective mass of the exciton and is obtained by $(m_e \times m_h)/(m_e + m_h)$. Because the previous terahertz experimental results show that carrier-transport properties are almost completely unaffected by the isotope effect (which means that the carrier effective masses are not notably affected), the main factor that affects the exciton binding energy is the dielectric constant. We then conducted density functional theory (DFT) calculations of the dielectric constant for a MAPbI$_3$ unit cell with the C−N axis of MA$^+$ in different directions (see the Experimental Methods section). As

listed in Table 1, the dielectric constants depend distinctly on the momentary directions of the C−N axis with respect to crystallographic planes (namely, the orientations of MA⁺). Thus, MA⁺ rotation changes the dielectric constants of the material and influences the exciton binding energy. However, because exciton binding energy in MAPbI₃ has been experimentally measured to be very small (only about 10 meV or less at room temperature), free charge carriers are directly generated upon light absorption at ambient condition.[41,49] Therefore, the dielectric-induced variation (less than a factor of 2 according to eq 1 and Table 1) in exciton binding energy is still less than kT (25.7 meV) at room temperature. Hence, the MA⁺ rotation-induced effect on exciton binding energy should not have any large impact on carrier lifetime. Nonetheless, our calculation still manifested a strong correlation between rotor orientation and dielectric constants in solid-state materials.

With the impact of excitons proven to be negligible on the carrier lifetime of MAPbI₃, we provide a potential mechanism to elucidate the root cause of deuteration-induced variation in carrier lifetime by investigating the polaron trapping effect that can lead to shallow traps in semiconductors.[50−52] Upon escaping from being bound with a hole in a polarizable semiconductor, a conduction electron attracts/repels multiple lattice cations/anions in its proximity via electrostatic interaction, leading to an electron−multi-ion entity called a polaron.[53] Apparently, high hole mobility facilitates polaron formation because the corresponding electron can overcome the recombination and interact with its neighboring lattice ions. In this manner, a shallow trap forms near the edge of the conduction band, in which the conduction electron can relax without recombination, leading to extended carrier lifetime.[54−57] In the case of MAPbI₃ single crystals, due to their excellent hole mobility[37] and low exciton binding energy,[41] the photoinduced electron can readily overcome recombination so as to interact with neighboring lattice ions. Recent theoretical work also implies that carriers in perovskites might be associated with polarons.[58] In particular, the rapid picosecond in-plane rotations of MA⁺ enable quick spatial reorientation of the cationic charge, so as to overlap their wave function with that of the free electron, forming a stably shallow trap that extends the carrier lifetime. Note that the MA⁺ cannot be a recombination center due to its poor electron affinity. In contrast, heavier CH₃ND₃⁺, CD₃NH₃⁺, and CD₃ND₃⁺ suffer from retarded rotation so as to decrease the probability of electrostatic overlap with the free electron; therefore, we observe shorter carrier lifetimes of deuterated perovskites. From the evidence, it is desirable to elucidate the dynamical relationship between MA⁺ orientations that are manifested as crystallographic planes and polaron trapping energies.

We conducted DFT calculations on the different polaron trapping energies when the C−N axis respectively pointed to the three representative crystallographic planes [100], [110], and [111] in a MAPbI₃ unit cell. The electronic structures near the band edge of MAPbI₃ generally reflect the trapping states for photogenerated carriers, and therefore, we show the calculated density of states (DOS) near the band edges of CH₃NH₃PbI₃ with CH₃NH₃⁺ along different crystallographic directions. The results are shown in Figure 4 and summarized in Table 2. As can be seen, the DOS near the valence band edge depends significantly on the orientation of CH₃NH₃⁺, and the differences for CH₃NH₃⁺ along the [100] (Figure 4a), [110] (Figure 4b), and [111] (Figure 4c) directions are especially
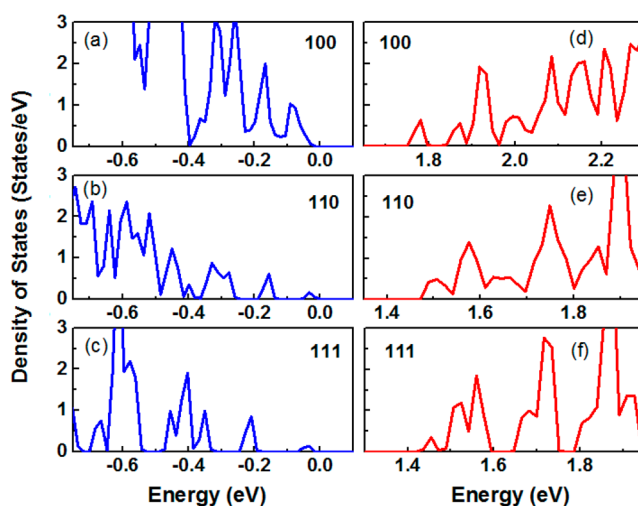

Figure 4. DOS near the band edge of CH₃NH₃PbI₃ with CH₃NH₃⁺ along different crystallographic directions including 100, 110, and 111. (a−c) DOS near the valence band edge. (d−f) DOS near the conduction band edge.

Table 2. Polaron Trapping Energy [meV] for Electron and Hole with Different C−N Pointing Directions

crystallographic planes	electron (meV)	hole (meV)
100	117	7
110	225	71
111	151	20

remarkable. This means that the hole trapping states will depend strongly on the orientation of CH₃NH₃⁺ in CH₃NH₃PbI₃. Furthermore, similar results also occur for the electron trapping states, as shown in Figures 4d−f and Table 2. As can be seen, [110] corresponds to the greatest trapping energies for both electrons (225 meV) and holes (71 meV), whereas [100] corresponds to the smallest trapping energies for both electrons (117 meV) and holes (7 meV). Hence, faster rotation of MA⁺ gives rise to a greater incidence of orienting the C−N axis along the [110] direction, which is associated with the greatest polaron trapping energy for both electrons and holes compared to the slow rotation of deuterated MA⁺, taking into account the effect of anisotropic alignments of MA⁺. Therefore, the lightest CH₃NH₃⁺ is more effective in trapping photoexcited electrons than any of its heavier isotopic counterparts; consequently, this results in the relatively longer carrier lifetime in CH₃NH₃PbI₃. To give a quantitative ratio of the in-plane rotational frequencies around the C−N axis of the four isotopes of MA⁺, we use the rigid free-rotor model in quantum mechanics, and the estimated frequency ratio is $\nu(CH_3NH_3^+)/\nu(CH_3ND_3^+)/\nu(CD_3NH_3^+)/\nu(CD_3ND_3^+) \approx$ 1:0.85:0.85:0.76, with the assumption that they take on the same rotational quantum state (see the Supporting Information for detailed calculation). Apparently, the trend of the in-plane rotational frequencies of the four isotopes of MA⁺ agrees well with the trend found in their carrier lifetimes, that is, $\tau(CH_3NH_3^+) > \tau(CH_3ND_3^+) \approx \tau(CD_3NH_3^+) > \tau(CD_3ND_3^+)$. Therefore, it is reasonable to state that the carrier lifetime in MAPbI₃ has strong dependency on the rotational frequency of the organic rotor MA⁺, and such an electron-rotor interaction is implemented via polaron formation involving the conduction electrons in the inorganic anionic framework and the asymmetric cationic charge on the organic rotors.

In summary, we discovered a new type of electron−lattice interaction, namely, an electron−rotor interaction, occurring in solid-state hybrid perovskite lead triiodide, whose structure is configured as asymmetric cationic MA$^+$ rotors electrostatically pinned in the cages formed by the anionic PbI$_3^-$ framework. The coupling between the cationic side of the rotors and the light-induced free electrons in the PbI$_3^-$ framework, as the formation of polarons, is effectively dependent on the rotational momentum of the rotors. This is evidenced by a TRPL study, in which the carrier lifetimes of isotopic hybrid perovskite lead triiodides exhibit a trend of CH$_3$NH$_3$PbI$_3$ > CH$_3$ND$_3$PbI$_3$ ≈ CD$_3$NH$_3$PbI$_3$ > CD$_3$ND$_3$PbI$_3$, in good agreement with the trend of their rotational frequencies. Theoretical work suggested that the orientation of the cationic rotors in perovskite structures can affect the charge separation states.[59,60]

Insightful understanding of electron−lattice interaction constitutes the mechanistic foundation for various energy transport, conversion, and storage sciences such as super-conductivity, thermoelectricity, photovoltaics, and supercapacitors. Therefore, the electron−rotor interaction discovered in solid-state semiconductors should help establish a theoretical foundation and provide an innovative alternative for better materials-by-design.

■ EXPERIMENTAL METHODS

Materials Synthesis. CH$_3$NH$_3$I was synthesized using the method described elsewhere.[61] CH$_3$ND$_3$I was made by dissolving pure CH$_3$NH$_3$I in excessive deuterium oxide (99.9 atom % D, Aldrich) at a 1:40 molar ratio in a 100 mL round-bottom flask, followed by rotary evaporation at 60 °C to dry off the solvent. This process was repeated four times to make sure that all active hydrogen atoms bonded to nitrogen were substituted by deuterium atoms. CD$_3$NH$_3$I was synthesized first by slowly reacting CD$_3$NH$_2$ gas (99.9 atom %, Aldrich) with an equimolar amount of HI in water (57 wt %, Aldrich) with constant stirring in a 500 mL round-bottom flask immersed in an ice bath, followed by rotary evaporation at 60 °C to dry off the solvent. CD$_3$NH$_3$I solid mixed with HI residue was then washed on filter paper six times with anhydrous ethyl ether (Fisher Chemical) accompanied by vacuum filtration each time. Washed CD$_3$NH$_3$I powder was dried in a vacuum oven at 80 °C overnight to further expel ethyl ether residue. The fully deuterated CD$_3$ND$_3$I was synthesized by dissolving the purified CD$_3$NH$_3$I as described above in excessive deuterium oxide at a 1:40 molar ratio in a 100 mL round-bottom flask, followed by rotary evaporation at 60 °C to dry off the solvent. This process was repeated four times to ensure complete substitution of ammonium hydrogen by deuterium to yield pure CD$_3$ND$_3$I. The CH$_3$NH$_3$I, CH$_3$ND$_3$I, CD$_3$NH$_3$I, and CD$_3$ND$_3$I samples obtained were further characterized by nuclear magnetic resonance (NMR) spectroscopy and mass spectrometry (MS) to ensure their purity, as shown in Figures S1−S6.

CH$_3$NH$_3$PbI$_3$, CH$_3$ND$_3$PbI$_3$, CD$_3$NH$_3$PbI$_3$, and CD$_3$ND$_3$PbI$_3$ single crystals were synthesized, respectively, by first mixing a 1:1 molar ratio of CH$_3$NH$_3$I, CH$_3$ND$_3$I, CD$_3$NH$_3$I, and CD$_3$ND$_3$I with lead(II) iodide (99.9985%, Alfa Aesar) in γ-butyrolactone (≥99%, Aldrich) in a glovebox to avoid possible exchange of hydrogen on nitrogen with moisture in air and material oxidation. The concentration of all of the resulting solutions was 1 M in terms of (CH$_3$NH$_3$I/ PbI$_2$), (CH$_3$ND$_3$I/PbI$_2$), (CD$_3$NH$_3$I/PbI$_2$), or (CD$_3$ND$_3$I/ PbI$_2$). Consequently, the solutions were heated at 110 °C for 3 h to produce small perovskite seed crystals of CH$_3$NH$_3$PbI$_3$,

CH$_3$ND$_3$PbI$_3$, CD$_3$NH$_3$PbI$_3$, and CD$_3$ND$_3$PbI$_3$, respectively. These seed crystals were then transferred to the corresponding fresh 1 M CH$_3$NH$_3$PbI$_3$, CH$_3$ND$_3$PbI$_3$, CD$_3$NH$_3$PbI$_3$, and CD$_3$ND$_3$PbI$_3$ solutions, respectively, for continuous growth for 48 h at 70 °C in darkness in argon without disturbance. The received single crystals were all stored in an argon atmosphere.

Materials Characterization. NMR spectroscopy was performed on a Bruker Spectrospin 300 MHz NMR spectrometer. Infrared spectroscopy of CH$_3$NH$_3$PbI$_3$ and CH$_3$ND$_3$PbI$_3$ single crystals was acquired on a Nicolet IR spectrometer at the BL01B beamline at the Shanghai Synchrotron Radiation Facility (SSRF). A mass spectrometry study was carried out using a Bruker Esquire 3000 quadrupole ion-trap mass spectrometer (Bruker Daltonics, Bremen, Germany) equipped with an electrospray ionization (ESI) source. All samples were introduced at a flow rate of 5 μL min^{-1}. The nebulizer gas, dry gas, needle voltage, and temperature were adjusted to 12 psi, 5.0 L/min, 4.5 kV, and 250 °C. All other tunable instrument parameters were optimized to give a maximum yield of the methylammonium ions. The tune file was maintained for all three sample acquisitions. Each sample run was acquired for about 2 min, resulting in over 100 scans. Averages were taken across the entire time frame. Synchrotron XRD experiments were performed at beamline 11BM, Advance Photon Source at Argonne National Laboratory. The instrument resolution is $\Delta d/d \approx 0.00017$, using 12 silicon (111) crystal analyzers positioned in front of the LaCl$_3$ scintillation detectors, representing the state-of-the-art *d*-spacing resolution for diffraction measurements.[62] Large single-crystal CH$_3$NH$_3$PbI$_3$, CH$_3$ND$_3$PbI$_3$, CD$_3$NH$_3$PbI$_3$, and CD$_3$ND$_3$PbI$_3$ were cracked into smaller single-crystal granules, which were tightly packed in a Krapton tube and tightly sealed with wax.

To measure static photoluminescence and time-resolved photoluminescence dynamics, single-crystal samples were photoexcited at 450 nm and 40 nJ/cm^2 via a 35 ps pulse width laser diode. PL photons were collected with a lens and directed to a 300 mm focal length grating spectrograph outfitted with a thermoelectrically cooled CCD and avalanche photodiode with time-correlated single-photon counting electronics.

Solar Cell Fabrications, Characterization, and Measurements. A fluorine-doped tin oxide (FTO) substrate (TEC 15, Hartford Glass Co) was patterned using the wet-etching method (zinc powder and HCl solution). Prepatterned FTO was cleaned and then deposited with a thin compact TiO$_2$ layer by spray pyrolysis using a 0.2 M titanium diisopropoxide bis-(acetylacetonate) in 1-butanol solution at 450 °C. The TiO$_2$ layer was annealed at 450 °C for 1 h. Perovskite films were prepared via the nonstoichiometric precursor method as reported before.[63] Briefly, organic salt (CH$_3$NH$_3$I or CH$_3$ND$_3$I)/PbI$_2$ = 1.2:1 was dissolved in a 1-methyl-2-pyrrolidinone/γ-butyrolactone (7/3, weight ratio) solution to form a 50 wt % precursor. The precursor was coated on top of the substrate by spin-coating at 4500 rpm for 25 s, and the wet film was immediately transferred into a diethyl ether (DEE, Fisher Chemical) bath for 90 s. Thermal annealing was processed at 150 °C for 20 min with a Petri dish covered on top under a low-humidity atmosphere. 2,2′,7,7′-Tetrakis(*N,N*-dimethoxyphenylamine)-9,9′-spirobifluorene (spiro-MeOTAD; Merck, Germany) was used as a hole-transport layer (HTL) by spin-coating a HTL solution, which consists of 80 mg of spiro-MeOTAD, 30 μL of bis(trifluoromethane) sulfonimide lithium salt stock solution (500 mg Li-TFSI in 1 mL

acetonitrile), 30 μL of 4-*tert*-butylpyridine (TBP), and 1 mL of chlorobenzene solvent, at 4000 rpm for 30 s. Finally, a 150 nm Ag layer was deposited on the HTL layer by thermal evaporation. The J–V characteristics of the cells, which have a 0.12 cm^2 masked area, were measured using a 2400 SourceMeter (Keithley) under simulated one-sun AM 1.5G illumination (100 mW cm^{-2}) (Oriel Sol3A Class AAA solar simulator, Newport Corporation). The incident photon-to-current efficiency (IPCE) was measured using a solar cell quantum efficiency measurement system (QEX10, PV Measurements). Stabilized power output was recorded by a potentiostat (VersaSTAT MC, Princeton Applied Research) near a maximum power output point. Thin-film surface morphology images were taken by using a Quanta 600 scanning electron microscope.

The time-resolved terahertz (THz) measurement is based on the Ti:sapphire ultrafast laser amplifier (800 nm, pulse duration $\approx$ 130 fs, $\sim$3 mJ/pulse, and 1 kHz repetition rate). The fundamental beam (800 nm) is split into two beams. One beam is sent to a TOPAS optical parametric amplifier to generate the pump pulse with a tunable wavelength, and its intensity is attenuated by a neutral-density filter. For this experiment, we employed a pump wavelength of 400 nm. The other beam is further split into two portions. One portion strikes a ZnTe crystal to generate a THz pulse that is focused on the sample. The other portion is directed along with the transmitted THz to another ZnTe crystal for the THz detection. The detailed working principle can be found in the literature.[64] The carrier lifetimes in perovskite thin films were studied by TRPL decays measured with a time-correlated single-photon counting system using a Fianium Supercontinuum high-power broad-band fiber filter (SC400-2-PP). The illumination spot size was about 0.02 mm^2 with $\sim$25 μW excitation at a wavelength of 500 nm.

Theoretical Calculation. The DFT calculations are conducted using the Vienna ab initio simulation package code.[65] The ionic potentials are described by the projector augmented wave (PAW) method within the generalized gradient approximation (GGA);[66] the long-range van der Waal's interactions are also taken into account by the empirical Grimme's method.[67] The plane-wave cutoff energy is 500 eV. In structural optimization, both the lattice vector and atomic positions are fully relaxed until the residual Hellmann−Feynman forces become smaller than 0.02 eV/Å. To investigate the polaronic effect, a $3 \times 3 \times 3$ supercell model of MAPbI$_3$ is used, the Brillouin zone is sampled with only the gamma point considering the large size of the model, and the polaron trapping energy is defined as the energy difference between the delocalized state of the carrier without structural distortion and the localized (trapped) state of the carrier with full structural optimization. For DOS calculation, the MAPbI$_3$ unit cell is used and the Brillouin zone is sampled with gamma-centered *k*-points. The dielectric constants are obtained by density functional perturbation theory using the linear response method.

ASSOCIATED CONTENT

Ⓢ Supporting Information

The Supporting Information is available free of charge on the ACS Publications website at DOI: 10.1021/acs.jpclett.6b01199.

Nuclear magnetic resonance, mass spectra, X-ray diffraction (XRD), scanning electron microscopy (SEM), complete UV−vis absorbance spectra, steady-state power output, single-crystal SEM, synchrotron high-resolution XRD, infrared spectra, and calculation of the ratio of rotational frequencies of MA$^+$ (PDF)

AUTHOR INFORMATION

Corresponding Authors
*E-mail: liugang@hpstar.ac.cn (G.L.).
*E-mail. Kai.Zhu@nrel.gov (K.Z.).
*E-mail. txu@niu.edu (T.X.).

Author Contributions
#J.G. and M.Y. contributed equally to this work.

Notes
The authors declare no competing financial interest.

REFERENCES

(1) Giri, G.; Verploegen, E.; Mannsfeld, S. C. B.; Atahan-Evrenk, S.; Kim, D. H.; Lee, S. Y.; Becerril, H. A.; Aspuru-Guzik, A.; Toney, M. F.; Bao, Z. Tuning Charge Transport in Solution-Sheared Organic Semiconductors Using Lattice Strain. *Nature* **2011**, *480*, 504−508.

(2) Bakulin, A. A.; Lovrincic, R.; Yu, X.; Selig, O.; Bakker, H. J.; Rezus, Y. L. A.; Nayak, P. K.; Fonari, A.; Coropceanu, V.; Brédas, J.-L.; et al. Mode-Selective Vibrational Modulation of Charge Transport in Organic Electronic Devices. *Nat. Commun.* **2015**, *6*, 7880.

(3) Reznik, D.; Pintschovius, L.; Ito, M.; Iikubo, S.; Sato, M.; Goka, H.; Fujita, M.; Yamada, K.; Gu, G. D.; Tranquada, J. M. Electron-Phonon Coupling Reflecting Dynamic Charge Inhomogeneity in Copper Oxide Superconductors. *Nature* **2006**, *440*, 1170−1173.

(4) Lanzara, A.; Bogdanov, P. V.; Zhou, X. J.; Kellar, S. A.; Feng, D. L.; Lu, E. D.; Yoshida, T.; Eisaki, H.; Fujimori, A.; Kishio, K.; et al. Evidence for Ubiquitous Strong Electron-Phonon Coupling in High-Temperature Superconductors. *Nature* **2001**, *412*, 510−514.

(5) Tisdale, W. A.; Williams, K. J.; Timp, B. A.; Norris, D. J.; Aydil, E. S.; Zhu, X.-Y. Hot-Electron Transfer from Semiconductor Nanocrystals. *Science* **2010**, *328*, 1543−1547.

(6) Roulleau, P.; Baer, S.; Choi, T.; Molitor, F.; Güttinger, J.; Müller, T.; Dröscher, S.; Ensslin, K.; Ihn, T. Coherent Electron-Phonon Coupling in Tailored Quantum Systems. *Nat. Commun.* **2011**, *2*, 239.

(7) Driza, N.; Blanco-Canosa, S.; Bakr, M.; Soltan, S.; Khalid, M.; Mustafa, L.; Kawashima, K.; Christiani, G.; Habermeier, H.-U.; Khaliullin, G.; et al. Long-Range Transfer of Electron-Phonon Coupling in Oxide Superlattices. *Nat. Mater.* **2012**, *11*, 675−681.

(8) Zhang, X.-L.; Liu, W.-M. Electron-Phonon Coupling and Its Implication for the Superconducting Topological Insulators. *Sci. Rep.* **2015**, *5*, 8964.

(9) Boschker, H.; Richter, C.; Fillis-Tsirakis, E.; Schneider, C. W.; Mannhart, J. Electron-Phonon Coupling and the Superconducting Phase Diagram of the LaAlO₃-SrTiO₃ Interface. *Sci. Rep.* **2015**, *5*, 12309.

(10) Weig, E. M.; Blick, R. H.; Brandes, T.; Kirschbaum, J.; Wegscheider, W.; Bichler, M.; Kotthaus, J. P. Single-Electron-Phonon Interaction in a Suspended Quantum Dot Phonon Cavity. *Phys. Rev. Lett.* **2004**, *92*, 046804.

(11) Leguy, A. M. A.; Frost, J. M.; McMahon, A. P.; Sakai, V. G.; Kochelmann, W.; Law, C.; Li, X.; Foglia, F.; Walsh, A.; O'Regan, B. C.; et al. The Dynamics of Methylammonium Ions in Hybrid Organic-Inorganic Perovskite Solar Cells. *Nat. Commun.* **2015**, *6*, 7124.

(12) Mosconi, E.; Quarti, C.; Ivanovska, T.; Ruani, G.; De Angelis, F. Structural and Electronic Properties of Organo-Halide Lead Perovskites: a Combined IR-Spectroscopy and *Ab Initio* Molecular Dynamics Investigation. *Phys. Chem. Chem. Phys.* **2014**, *16*, 16137−16144.

(13) Meloni, S.; Moehl, T.; Tress, W.; Franckevičius, M.; Saliba, M.; Lee, Y. H.; Gao, P.; Nazeeruddin, M. K.; Zakeeruddin, S. M.; Rothlisberger, U.; et al. Ionic Polarization-Induced Current-Voltage Hysteresis in $CH_3NH_3PbX_3$ Perovskite Solar Cells. *Nat. Commun.* **2016**, *7*, 10334.

(14) Pérez-Osorio, M. A.; Milot, R. L.; Filip, M. R.; Patel, J. B.; Herz, L. M.; Johnston, M. B.; Giustino, F. Vibrational Properties of the Organic-Inorganic Halide Perovskite $CH_3NH_3PbI_3$ from Theory and Experiment: Factor Group Analysis, First-Principles Calculations, and Low-Temperature Infrared Spectra. *J. Phys. Chem. C* **2015**, *119*, 25703−25718.

(15) Motta, C.; El-Mellouhi, F.; Kais, S.; Tabet, N.; Alharbi, F.; Sanvito, S. Revealing the Role of Organic Cations in Hybrid Halide Perovskite $CH_3NH_3PbI_3$. *Nat. Commun.* **2015**, *6*, 7026.

(16) Chen, T.; Foley, B. J.; Ipek, B.; Tyagi, M.; Copley, J. R. D.; Brown, C. M.; Choi, J. J.; Lee, S.-H. Rotational Dynamics of Organic Cations in the $CH_3NH_3PbI_3$ Perovskite. *Phys. Chem. Chem. Phys.* **2015**, *17*, 31278−31286.

(17) Mattoni, A.; Filippetti, A.; Saba, M. I.; Delugas, P. Methylammonium Rotational Dynamics in Lead Halide Perovskite by Classical Molecular Dynamics: the Role of Temperature. *J. Phys. Chem. C* **2015**, *119*, 17421−17428.

(18) Bakulin, A. A.; Selig, O.; Bakker, H. J.; Rezus, Y. L. A.; Müller, C.; Glaser, T.; Lovrincic, R.; Sun, Z.; Chen, Z.; Walsh, A.; et al. Real-Time Observation of Organic Cation Reorientation in Methylammonium Lead Iodide Perovskites. *J. Phys. Chem. Lett.* **2015**, *6*, 3663−3669.

(19) Frost, J. M.; Butler, K. T.; Brivio, F.; Hendon, C. H.; van Schilfgaarde, M.; Walsh, A. Atomistic Origins of High-Performance in Hybrid Halide Perovskite Solar Cells. *Nano Lett.* **2014**, *14*, 2584−2590.

(20) Glaser, T.; Müller, C.; Sendner, M.; Krekeler, C.; Semonin, O. E.; Hull, T. D.; Yaffe, O.; Owen, J. S.; Kowalsky, W.; Pucci, A.; et al. Infrared Spectroscopic Study of Vibrational Modes in Methylammonium Lead Halide Perovskites. *J. Phys. Chem. Lett.* **2015**, *6*, 2913−2918.

(21) Ganose, A. M.; Savory, C. N.; Scanlon, D. O. $(CH_3NH_3)_2Pb(SCN)_2I_2$: a More Stable Structural Motif for Hybrid Halide Photovoltaics? *J. Phys. Chem. Lett.* **2015**, *6*, 4594−4598.

(22) Baikie, T.; Fang, Y.; Kadro, J. M.; Schreyer, M.; Wei, F.; Mhaisalkar, S. G.; Graetzel, M.; White, T. J. Synthesis and Crystal Chemistry of the Hybrid Perovskite $(CH_3NH_3)PbI_3$ for Solid-State Sensitized Solar Cell Applications. *J. Mater. Chem. A* **2013**, *1*, 5628−5641.

(23) Zhao, T.; Shi, W.; Xi, J.; Wang, D.; Shuai, Z. Intrinsic and Extrinsic Charge Transport in $CH_3NH_3PbI_3$ Perovskites Predicted from First-Principles. *Sci. Rep.* **2016**, *7*, 19968.

(24) Liao, W.-Q.; Zhang, Y.; Hu, C.-L.; Mao, J.-G.; Ye, H.-Y.; Li, P.-F.; Huang, S. D.; Xiong, R.-G. A Lead-Halide Perovskite Molecular Ferroelectric Semiconductor. *Nat. Commun.* **2015**, *6*, 7338.

(25) Kaltenbrunner, M.; Adam, G.; Glowacki, E. D.; Drack, M.; Schwödiauer, R.; Leonat, L.; Apaydin, D. H.; Groiss, H.; Scharber, M. C.; White, M. S.; et al. Flexible High Power-Per-Weight Perovskite Solar Cells with Chromium Oxide-Metal Contacts for Improved Stability in Air. *Nat. Mater.* **2015**, *14*, 1032−1039.

(26) Li, X.; Dar, I.; Yi, C.; Luo, J.; Tschumi, M.; Zakeeruddin, S. M.; Nazeeruddin, M. K.; Han, H.; Grätzel, M. Improved Performance and Stability of Perovskite Solar Cells by Crystal Crosslinking with Alkylphosphonic Acid ω-Ammonium Chlorides. *Nat. Chem.* **2015**, *7*, 703−711.

(27) You, J.; Meng, L.; Song, T.-B.; Guo, T.-F.; Yang, Y.; Chang, W.-H.; Hong, Z.; Chen, H.; Zhou, H.; Chen, Q.; et al. Improved Air Stability of Perovskite Solar Cells via Solution-Processed Metal Oxide Transport Layers. *Nat. Nanotechnol.* **2015**, *11*, 75−81.

(28) Guerrero, A.; You, J.; Aranda, C.; Kang, Y. S.; Garcia-Belmonte, G.; Zhou, H.; Bisquert, J.; Yang, Y. Interfacial Degradation of Planar Lead Halide Perovskite Solar Cells. *ACS Nano* **2016**, *10*, 218−224.

(29) Babayigit, A.; Thanh, D. D.; Ethirajan, A.; Manca, J.; Muller, M.; Boyen, H.-G.; Conings, B. Assessing the Toxicity of Pb- and Sn-Based Perovskite Solar Cells in Model Organism Danio rerio. *Sci. Rep.* **2016**, *6*, 18721.

(30) Yang, S.; Wang, Y.; Liu, P.; Cheng, Y.-B.; Zhao, H. J.; Yang, H. G. Functionalization of Perovskite Thin Films with Moisture-Tolerant Molecules. *Nat. Energy* **2016**, *1*, 15016.

(31) Göbel, A.; Ruf, T.; Cardona, M.; Lin, C. T.; et al. Effects of the Isotopic Composition on the Fundamental Gap of CuCl. *Phys. Rev. B: Condens. Matter Mater. Phys.* **1998**, *57*, 15183−15190.

(32) Shao, M.; Keum, J.; Chen, J.; He, Y.; Chen, W.; Browning, J. F.; Jakowski, J.; Sumpter, B. G.; Ivanov, I. N.; Ma, Y.-Z.; et al. The Isotopic Effects of Deuteration on Optoelectronic Properties of Conducting Polymers. *Nat. Commun.* **2014**, *5*, 3180.

(33) Ostroverkhova, O.; Cooke, D. G.; Shcherbyna, S.; Egerton, R. F.; Hegmann, F. A.; Tykwinski, R. R.; Anthony, J. E. Bandlike Transport in Pentacene and Functionalized Pentacene Thin Films Revealed by Subpicosecond Transient Photoconductivity Measurements. *Phys. Rev. B: Condens. Matter Mater. Phys.* **2005**, *71*, 035204.

(34) Yang, Y.; Yan, Y.; Yang, M.; Choi, S.; Zhu, K.; Luther, J. M.; Beard, M. C. Low Surface Recombination Velocity in Solution-Grown $CH_3NH_3PbBr_3$ Perovskite Single Crystal. *Nat. Commun.* **2015**, *6*, 7961.

(35) Wehrenfennig, C.; Liu, M.; Snaith, H. J.; Johnston, M. B.; Herz, L. M. Charge-Carrier Dynamics in Vapour-Deposited Films of the Organolead Halide Perovskite $CH_3NH_3PbI_{3-x}Cl_x$. *Energy Environ. Sci.* **2014**, *7*, 2269−2275.

(36) Tian, W.; Zhao, C.; Leng, J.; Cui, R.; Jin, S. Visualizing Carrier Diffusion in Individual Single-Crystal Organolead Halide Perovskite Nanowires and Nanoplates. *J. Am. Chem. Soc.* **2015**, *137*, 12458−12461.

(37) Shi, D.; Adinolfi, V.; Comin, R.; Yuan, M.; Alarousu, E.; Buin, A.; Chen, Y.; Hoogland, S.; Rothenberger, A.; Katsiev, K.; et al. Low Trap-State Density and Long Carrier Diffusion in Organolead Trihalide Perovskite Single Crystals. *Science* **2015**, *347*, 519−522.

(38) Yang, Y.; Ostrowski, D. P.; France, R. M.; Zhu, K.; van de Lagemaat, J.; Luther, J. M.; Beard, M. C. Observation of a Hot-Phonon Bottleneck in Lead-Iodide Perovskites. *Nat. Photonics* **2015**, *10*, 53−59.

(39) La-o-vorakiat, C.; Salim, T.; Kadro, J.; Khuc, M.-T.; Haselsberger, R.; Cheng, L.; Xia, H.; Gurzadyan, G. G.; Su, H.; Lam, Y. M.; et al. Elucidating the Role of Disorder and Free-Carrier Recombination Kinetics in $CH_3NH_3PbI_3$ Perovskite Films. *Nat. Commun.* **2015**, *6*, 7903.

(40) Chen, B.; Yang, M.; Priya, S.; Zhu, K. Origin of *J-V* Hysteresis in Perovskite Solar Cells. *J. Phys. Chem. Lett.* **2016**, *7*, 905−917.

(41) Miyata, A.; Mitioglu, A.; Plochocka, P.; Portugall, O.; Wang, J. T-W.; Stranks, S. D.; Snaith, H. J.; Nicholas, R. J. Direct Measurement of the Exciton Binding Energy and Effective Masses for Charge Carriers in Organic-Inorganic Tri-Halide Perovskites. *Nat. Phys.* **2015**, *11*, 582−587.

(42) Li, Y.; Meng, L.; Yang, Y.; Xu, G.; Hong, Z.; Chen, Q.; You, J.; Li, G.; Yang, Y.; Li, Y. High-Efficiency Robust Perovskite Solar Cells on Ultrathin Flexible Substrates. *Nat. Commun.* **2016**, *7*, 10214.

(43) Zhu, H.; Fu, Y.; Meng, F.; Wu, X.; Gong, Z.; Ding, Q.; Gustafsson, M. V.; Trinh, M. T.; Jin, S.; Zhu, X.-Y. Lead Halide Perovskite Nanowire Lasers with Low Lasing Thresholds and High Quality Factors. *Nat. Mater.* **2015**, *14*, 636−642.

(44) Mattoni, A.; Filippetti, A.; Saba, M. I.; Caddeo, C.; Delugas, P. Temperature Evolution of Methylammonium Trihalide Vibrations at the Atomic Scale. *J. Phys. Chem. Lett.* **2016**, *7*, 529−535.

(45) Egger, D. A.; Kronik, L.; Rappe, A. M. Theory of Hydrogen Migration in Organic-Inorganic Halide Perovskites. *Angew. Chem., Int. Ed.* **2015**, *54*, 12437−12441.

(46) Saidaminov, M. I.; Abdelhady, A. L.; Murali, B.; Alarousu, E.; Burlakov, V. M.; Peng, W.; Dursun, I.; Wang, L.; He, Y.; Maculan, G.; et al. High-Quality Bulk Hybrid Perovskite Single Crystals within Minutes by Inverse Temperature Crystallization. *Nat. Commun.* **2015**, *6*, 7586.

(47) Dong, Q.; Fang, Y.; Shao, Y.; Mulligan, P.; Qiu, J.; Cao, L.; Huang, J. Electron-Hole Diffusion Lengths > 175 μm in Solution-Grown $CH_3NH_3PbI_3$ Single Crystals. *Science* **2015**, *347*, 967−970.

(48) Yaffe, O.; Chernikov, A.; Norman, Z. M.; Zhong, Y.; Velauthapillai, A.; van der Zande, A.; Owen, J. S.; Heinz, T. F. Excitons in Ultrathin Organic-Inorganic Perovskite Crystals. *Phys. Rev. B: Condens. Matter Mater. Phys.* **2015**, *92*, 045414.

(49) D'Innocenzo, V.; Grancini, G.; Alcocer, M. J. P.; Kandada, A. R. S.; Stranks, S. D.; Lee, M. M.; Lanzani, G.; Snaith, H. J.; Petrozza, A. Excitons versus Free Charges in Organo-Lead Tri-Halide Perovskites. *Nat. Commun.* **2014**, *5*, 3586.

(50) Stoneham, A. M.; Gavartin, J.; Shluger, A. L.; Kimmel, A. V.; Muñoz Ramo, D.; Rønnow, H. M.; Aeppli, G.; Renner, C. Trapping, Self-Trapping and the Polaron Family. *J. Phys.: Condens. Matter* **2007**, *19*, 255208.

(51) Gavartin, J. L.; Muñoz Ramo, D.; Shluger, A. L.; Bersuker, G.; Lee, B. H. Negative Oxygen Vacancies in HfO_2 as Charge Traps in High-k Stacks. *Appl. Phys. Lett.* **2006**, *89*, 082908.

(52) Gavartin, J. L.; Munoz Ramo, D.; Shluger, A.; Bersuker, G. Polaron-Like Charge Trapping in Oxygen Deficient and Disordered HfO_2: Theoretical Insight. *ECS Trans.* **2006**, *3*, 277−290.

(53) Sezen, H.; Shang, H.; Bebensee, F.; Yang, C.; Buchholz, M.; Nefedov, A.; Heissler, S.; Carbogno, C.; Scheffler, M.; Rinke, P.; et al. Evidence for Photogenerated Intermediate Hole Polarons in ZnO. *Nat. Commun.* **2015**, *6*, 6901.

(54) Sekhar, M. C.; Santhosh, K.; Praveen Kumar, J.; Mondal, N.; Soumya, S.; Samanta, A. CdTe Quantum Dots in Ionic Liquid: Stability and Hole Scavenging in the Presence of a Sulfide Salt. *J. Phys. Chem. C* **2014**, *118*, 18481−18487.

(55) Mondal, N.; Samanta, A. Ultrafast Charge Transfer and Trapping Dynamics in a Colloidal Mixture of Similarly Charged CdTe Quantum Dots and Silver Nanoparticles. *J. Phys. Chem. C* **2016**, *120*, 650−658.

(56) Fitzmorris, B. C.; Cooper, J. K.; Edberg, J.; Gul, S.; Guo, J.; Zhang, J. Z. Synthesis and Structural, Optical, and Dynamic Properties of Core/Shell/Shell CdSe/ZnSe/ZnS Quantum Dots. *J. Phys. Chem. C* **2012**, *116*, 25065−25073.

(57) Sekhar, M. C.; Samanta, A. Ultrafast Transient Absorption Study of the Nature of Interaction between Oppositely Charged Photoexcited CdTe Quantum Dots and Cresyl Violet. *J. Phys. Chem. C* **2015**, *119*, 15661−15668.

(58) Zhu, X.-Y.; Podzorov, V. Charge Carriers in Hybrid Organic−Inorganic Lead Halide Perovskites Might Be Protected as Large Polarons. *J. Phys. Chem. Lett.* **2015**, *6*, 4758−4761.

(59) Quarti, C.; Mosconi, E.; De Angelis, F. Interplay of Orientational Order and Electronic Structure in Methylammonium Lead Iodide: Implications for Solar Cell Operation. *Chem. Mater.* **2014**, *26*, 6557−6569.

(60) Liu, S.; Zheng, F.; Koocher, N. Z.; Takenaka, H.; Wang, F.; Rappe, A. M. Ferroelectric Domain Wall Induced Band Gap Reduction and Charge Separation in Organometal Halide Perovskites. *J. Phys. Chem. Lett.* **2015**, *6*, 693−699.

(61) Lee, M. M.; Teuscher, J.; Miyasaka, T.; Murakami, T. N.; Snaith, H. J. Efficient Hybrid Solar Cells Based on Meso-Superstructured Organometal Halide Perovskites. *Science* **2012**, *338*, 643−647.

(62) Lee, P. L.; Shu, D.; Ramanathan, M.; Preissner, C.; Wang, J.; Beno, M. A.; Von Dreele, R. B.; Ribaud, L.; Kurtz, C.; Antao, S. M.; et al. A Twelve-Analyzer Detector System for High-Resolution Powder Diffraction. *J. Synchrotron Radiat.* **2008**, *15*, 427−432.

(63) Yang, M.; Zhou, Y.; Zeng, Y.; Jiang, C.-S.; Padture, N. P.; Zhu, K. Square-Centimeter Solution-Processed Planar $CH_3NH_3PbI_3$ Perovskite Solar Cells with Efficiency Exceeding 15%. *Adv. Mater.* **2015**, *27*, 6363−6370.

(64) Beard, M. C.; Turner, G. M.; Schmuttenmaer, C. A. Transient Photoconductivity in GaAs as Measured by Time-Resolved Terahertz Spectroscopy. *Phys. Rev. B: Condens. Matter Mater. Phys.* **2000**, *62*, 15764.

(65) Kresse, G.; Furthmüller, J. Efficient Iterative Schemes for *Ab Initio* Total-Energy Calculations Using a Plane-Wave Basis Set. *Phys. Rev. B: Condens. Matter Mater. Phys.* **1996**, *54*, 11169−11186.

(66) Perdew, J. P.; Burke, K.; Ernzerhof, M. Generalized Gradient Approximation Made Simple. *Phys. Rev. Lett.* **1996**, *77*, 3865.

(67) Grimme, S. Semiempirical GGA-Type Density Functional Constructed with a Long-Range Dispersion Correction. *J. Comput. Chem.* **2006**, *27*, 1787−1799.